Atmospheric
Chemistry
and Physics

Supplement of

Aerosol optical properties at SORPES in Nanjing, east China

Yicheng Shen et al.

Correspondence to: Aijun Ding (dingaj@nju.edu.cn) and Aki Virkkula (aki.virkkula@fmi.fi)

S1. Evaluation of humidity corrections

Figure S1 presents a brief evaluation on hygroscopic enhancement correction. Monthly averaged σ_{sp} and b before and after correction are compared. In summer, the internal heater was often not working properly and majority of summer data were corrected according to the parameterization presented in section 2.3.1. Two sets of c and g are compared. In revised manuscript, c and g are set to 0.72 and 0.65 for total scattering and 0.87 and 0.34 for backscattering coefficient. These values were taken from Carrico et al. (2003). The correction of Zhang et al. (2016) was only used for comparison and will no longer be used in revised manuscript. The c and g for total scattering are 0.85 and 0.29 respectively and backscatter scattering fraction is corrected using piecewise linear interpolation since they provide f(RH)$_{bsp}$ for some certain RHs. We did this change for 2 reasons. On one hand, Carrico's paper also includes equations for correcting backscattering coefficient, which is important for correcting backscattering fraction. On the other hand, Zhang et al. (2013) has a shorter experiment period and states that their result is quite different from other works, we choose not to use their result.
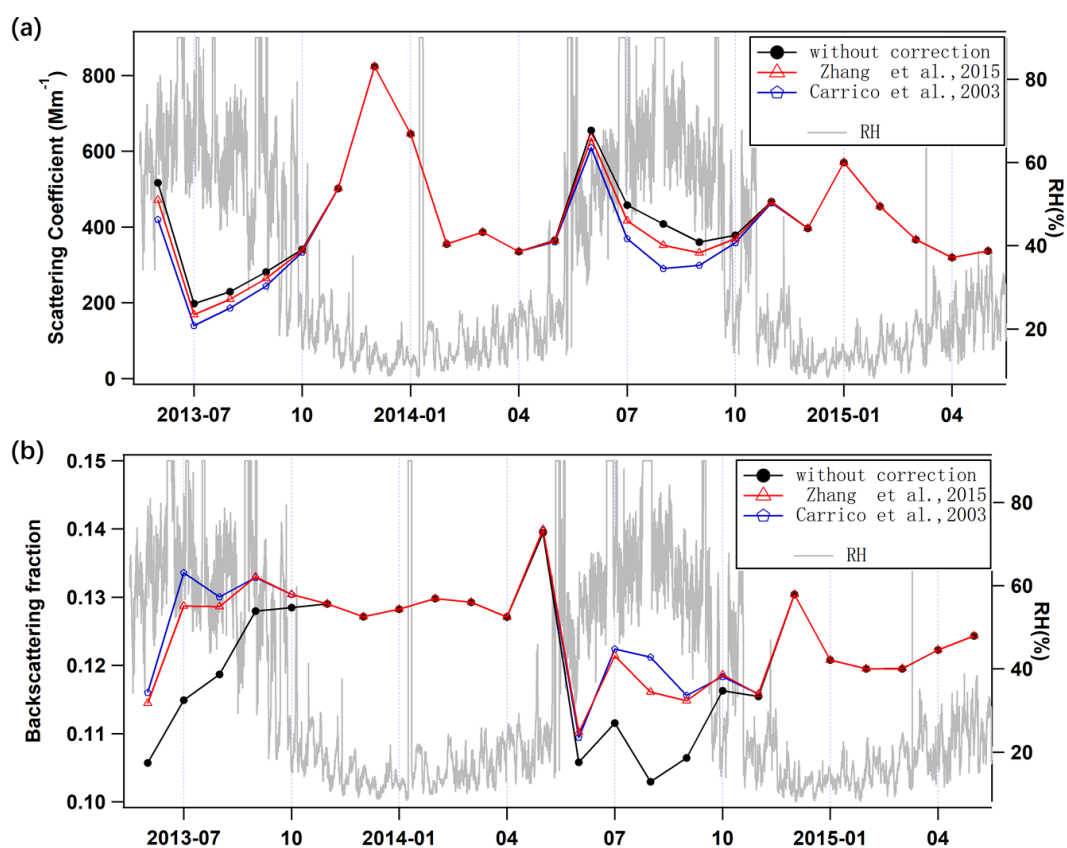

Figure S1. Effects of two humidity corrections on monthly-averaged (a) total scattering coefficient and (b) backscatter fraction at $\lambda = 525$ nm. The grey line shows the hourly-averaged relative humidity of sample air.

The monthly average total scattering coefficient is slightly changed for June, July, August, September, and October, and unchanged for the rest of the year. Time variation of the monthly averaged uncorrected data is similar to monthly-averaged corrected data for both settings. Thus we suggest the potential artifact brought from the correction is limited and will not jeopardize the discussion and result concerning σ_{sp}. For the correction of backscatter fraction, correction using both methods were consistent with each other

while both corrected results were evidently different from the uncorrected data for summertime. The correction for backscattering coefficient might bring a larger artifact than the correction of σ_{sp}.

S2. Comparisons of measured and modeled scattering coefficients

A quality control of the scattering data was obtained by using theoretical calculations based on Mie theory and size distributions. The Mie code by Bohren and Huffman was used for the modeling. The calculations were done by using the hourly-averaged size distribution data measured with the DMPS in the size range of 6 – 800 nm mobility diameter. The refractive index of ammonium sulfate 1.52 + 0i was used for all sizes distributions and all sizes. The code yelds both total scattering and backscattering coefficients. They were compared with the hourly-averaged nephelometer data corrected for humidity as described above. The period of the closure study is as same as that mentioned in the main article, excluding 09/12/2014~30/03/2015 (111days, 15.2% of the entire measurement period) when the DMPS was not working properly. The results are presented in Figure S2.
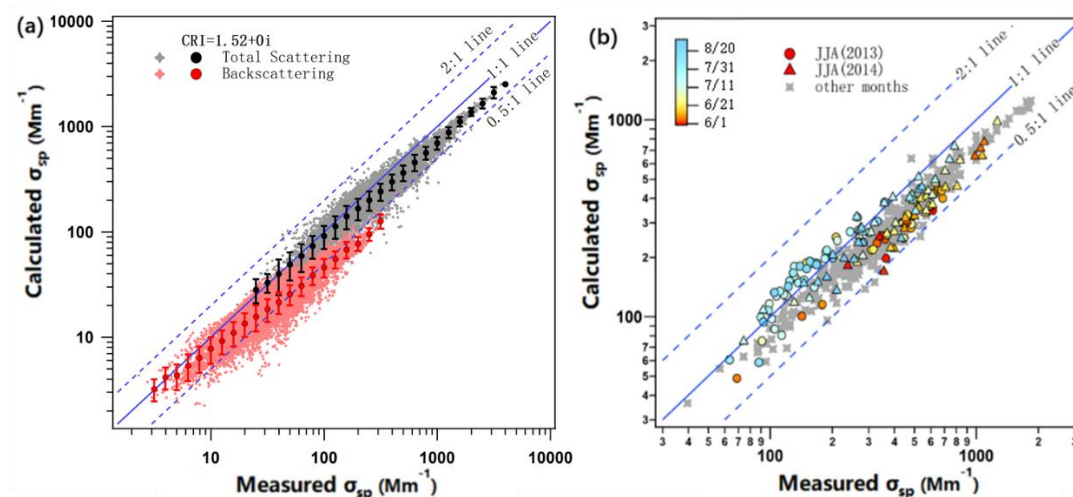

Figure S2. a) A comparison of measured and modeled hourly-averaged total scattering and backscattering coefficients at λ = 525 nm. Black and grey symbols: total scattering coefficient, red and pink symbols: backscattering coefficient. The circles represent the average modeled value in each logarithmically evenly-spaced bin of measured scattering and backscattering coefficient and the error bars the standard deviation of the same range. b) A comparison of measured and modeled daily-averaged total scattering coefficients at λ = 525 nm. The color-coded points are for summer (JJA in 2013 and 2014 respectively). All modeled scattering and backscattering coefficients were modeled using the refractive index of ammonium sulfate (m = 1.52 + 0i).

The comparison shows that when total scattering coefficient is lower, the modeled value is close to the measured value. When scattering coefficient is high, the modeled value is lower than the measured value, similar to the relationship of the modeled and measured backscattering coefficient ($\sigma_{bsp,cal}$ and $\sigma_{bsp,mea}$). There are is many possible explanations of such a difference. Firstly, when scattering coefficient is high, there tend to be more particles whose sizes are beyond DMPS's range, so light scattering by those particles is omitted in the modeled scattering coefficient. Secondly, a fixed RI=1.52+0i is used for the calculation, however, as the aerosol secondary formation is usually accompanied by photochemical processes in SORPES, RI may to be underestimated when scattering coefficient is high. Thirdly, a

systematic bias of measurement may exist. Despite the difference discussed above, modeled and measured data generally match well, the linear correlation coefficient between $\sigma_{sp,cal}$ and $\sigma_{sp,mea}$ is 0.973 while the linear correlation coefficient between $\sigma_{bsp,cal}$ and $\sigma_{bsp,mea}$ is 0.925. We found that modeling backscattering coefficient is very sensitive to the refractive index, which may explain the lower correlation coefficient for backscattering.

Figure S2b is similar to S2a but uses daily-averaged data. Data measured in spring (MAM), autumn (SON) and winter (DJF) are colored gray. These data points are consistently concentrated along a line. The data in summer are more scattered. In June of both 2013 and 2014, the measured light scattering coefficient is higher than the modeled, while in July and August the measured is lower than the modeled. One possible explanation is that size distribution and chemical compositions were unique in June and in July/August compared to the rest of the year (discussed in chapter 3.2). However, we cannot rule out the possibility that summer data suffer from the higher relative humidity even after the humidity corrections. Thus, we treated summer data with more care when trying to draw conclusions.

S3. Comparison between scattering coefficients and PM$_{2.5}$ concentrations

Figure S3 shows the comparison of the humidity-corrected scattering coefficient vs. PM$_{2.5}$. The σ_{sp} is generally consistent with PM$_{2.5}$. The σ_{sp}–to–PM$_{2.5}$ ratio is the mass scattering efficiency (MSE). The lines presenting MSE = 4, 6 and 8 m^2 g^{-1} are also shown. The MSE is ~6 m^2 g^{-1} and almost all data are between 4 and 8 m^2 g^{-1}. The values are higher than the average of fine mode MSE of 3.6 ± 1.2 m^2 g^{-1} in the review by Hand and Malm (2007). However, in the same review there are some sites for which MSE in the range of ~$5 - 8$ m^2 g^{-1} for sulfates, nitrates and POM have been reported so the values obtained in the present study are not exceptional. In June MSE is higher than in other months which is possibly related to the special characteristics of aerosol in June or it may again be an indication of imperfect humidity correction of the nephelometer data. It should also be noted that the MSE used here is a ratio between σ_{sp} of TSP and PM$_{2.5}$, since the nephelometer's inlet had no cutoff size so they are covering different size ranges.
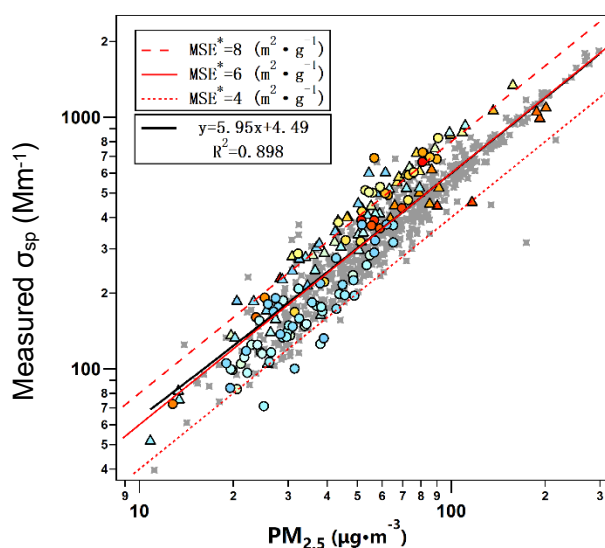

Figure S3. Comparison of daily-averaged humidity-corrected total scattering coefficient at $\lambda = 525$ nm and PM$_{2.5}$ concentrations. The color-coded points are for summer (JJA in 2013 and 2014 respectively) as in Fig S2. The red lines depict constant mass scattering efficiencies (MSE) of 4, 6, and 8 m^2 g^{-1}.

S4. Analyses of seasonal variations of modeled AOPs

In order to study, how much the seasonal cycles of the AOPs are affected by the uncertainty of the humidity correction of the nephelometer, the cycles were recalculated by using modeled scattering and measured absorption data. Figure S4 presents seasonal cycles of modeled of AOPs including modeled scattering coefficient (σ_{sp}*), Ångstrom Exponent for Scattering(SAE*), Single Scattering Albedo (SSA*) and backscatter fraction (b*). Here, SSA*= σ_{sp}*/(σ_{sp}*+σ_{ap}). SAE is calculated between 635 nm and 450 nm. The seasonal variation of modeled AOPs were generally consistent with those of the measured AOPs. For June, b* and SAE* are significantly lower than any other months while SSA* is highest of the year.

Even though the nephelometer data in summer are not as reliable as in the other months, the consistency of seasonal cycles suggests that all the discussion about the seasonality can be still considered to be valid.
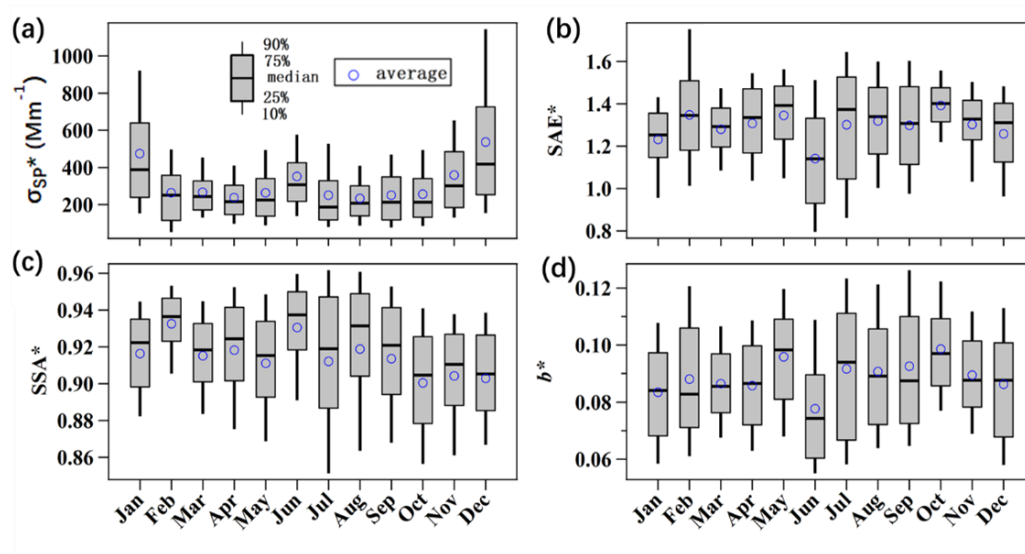

Figure S4. Seasonal variation of modeled a) total scattering coefficient at λ = 525 nm, b) scattering Ångström exponent (SAE), c) single-scattering albedo (SSA) at λ = 525 nm, and d) backscatter fraction at λ = 525 nm. The modeled data were calculated by using the DPMS data and the refractive index of amonium sulfate (m = 1.52 + 0i). In c) the absorption coefficients needed for the SSA were calculated from the Aethalometer data.

S5. Analyses of seasonal variations of emissions

A brief discussion about the seasonality of emission is necessary for better understanding of the seasonality of AOPs. The data used for discussion are MIX v1.1 gridded emissions of BC, $PM_{2.5}$, SO_2, and NO_x. The data can be downloaded on the homepage of Multi-resolution Emission Inventory for China (MEIC) (http://www.meicmodel.org/dataset-mix.html). Description of inventory can be found in Li et al. (2017). Figure S5a~d shows the yearly average BC, $PM_{2.5}$, SO_2, and NO_x emissions. $PM_{2.5}$ here is for primary $PM_{2.5}$. We used the ratio between January and July to describe the seasonality in   Fig. S5(e)~(h).
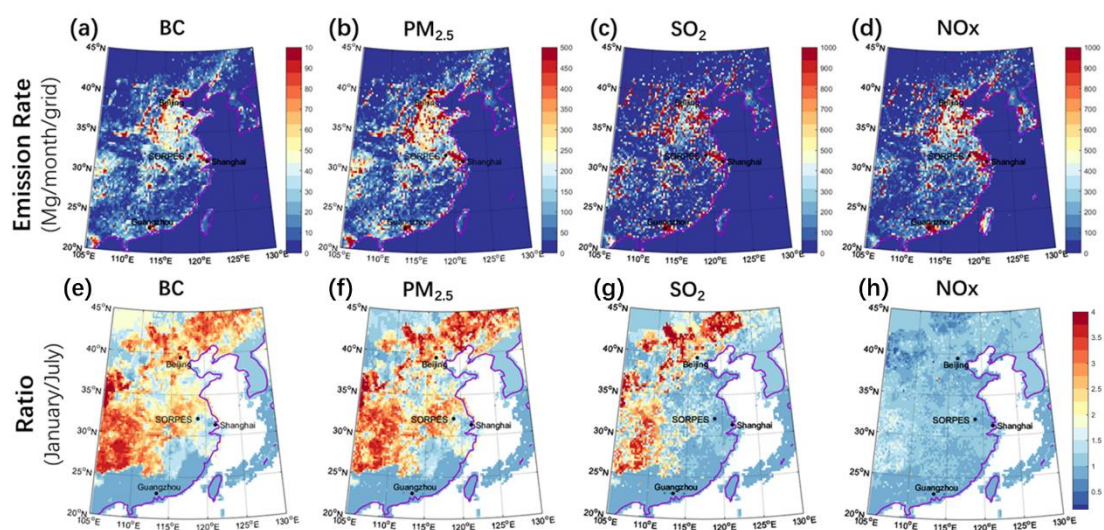

Figure S5. (a) – (d) Annual mean emission rates of BC, $PM_{2.5}$, SO_2 and NO_x, (e) – (f) seasonality of the emssion rates. The seasonality is here described as the ratios of the emission rates in January and July, which represent the highest and lowest emission rates of the year.

The effects of the emission seasonality on AOPs are not straightforward to explain: the emission rate and seasonality vary significantly from one grid another while the AOPs in SORPES is influenced by air mass coming from different locations. The emission inventory can give us some information about the potential effect of emission seasonality on AOPs, but not enough to draw any conclusion.

The emission of primary particles including BC and primary $PM_{2.5}$ have a strong seasonality in the center, north and north-east of China. In winter the emissions of BC and primary $PM_{2.5}$ are more than 4 times as much as in summer for many parts of China. However, in the center of YRD and southern China, there is no clear seasonality of BC and primary $PM_{2.5}$. Even the exact grid of SORPES shows on clear seasonality of BC and primary $PM_{2.5}$, the majority of surrounding areas tend to emit more BC and primary $PM_{2.5}$ in winter. This may be one contributor to the higher σ_{sp} and σ_{ap} in winter.

A large fraction of particles in SORPES are secondary compopouds such as sulfate and nitrate, the proxy of which are SO_2 and NO_x. The emission rate of SO_2 has a much weaker seasonality national-wide compared to BC. Both SO_2 and NO_x emitted near SORPES has a very weak seasonality. The seasonality of emission should have to decrease the SSA in winter which is not evident in Figure 3c.
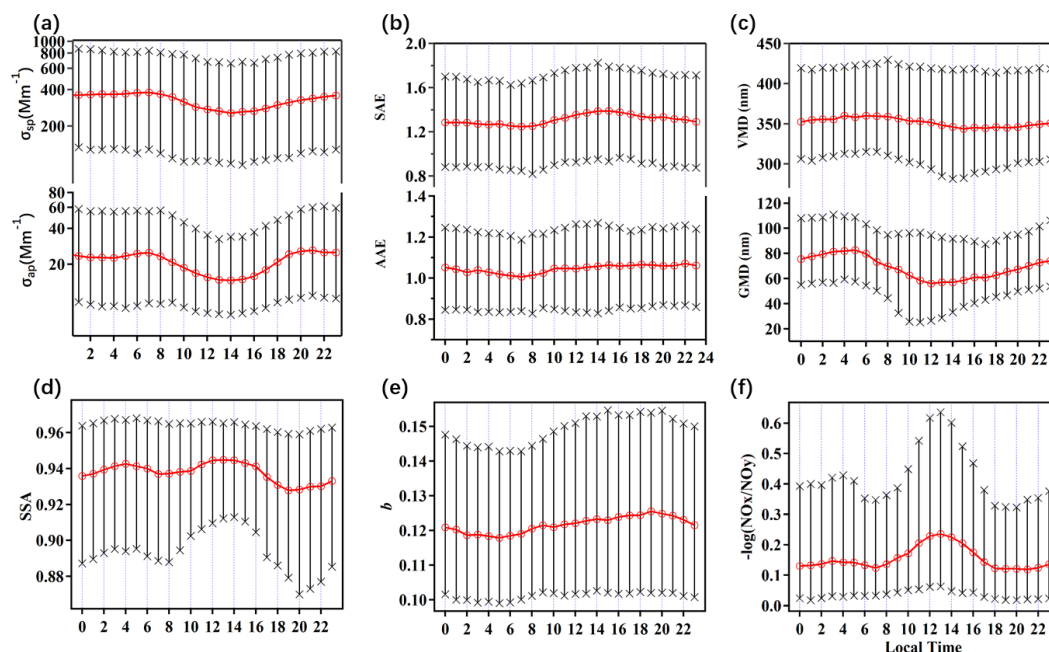
S6. Analyses of diurnal cycles

Figure S6. The same as Figure 4, but for different percentiles of 2-year averaged diurnal cycle. Black markers are for 10th and 90th percentile respectively, red line and cycles are for median value.

Figure S6 (a)~(h) are the 2-year-averaged diurnal cycles of AOPs with median, 10th and 90th percentiles. The 10th and 90th percentile, in general, vary consistently with the median line, and these three lines also consistent with the shape of the diurnal cycle of average values. This ruled out the possibility that some certain feature in diurnal cycles is artificial thus make the discussion about the diurnal variation more authentic.

The difference between 90th and 10th percentile is usually larger than the extent of diurnal variation (i.e. maximum-minimum). This is because AOPs varies more significant in multi-day scale pollution-episodes. Still, diurnal variation is, in general, clear and authentic.

S7. Additional discussions on the relationships between wind and AOPs

In this section we present additional discussions about the wind dependence of AOPs. We also involve some analyses of aerosol chemical composition and diurnal cycles of wind. The main goal is to evaluate reasons for the high σ_{sp} in the W-WNW sector and the high σ_{ap} in the S-SSE sector.

S7.1 σ_{sp} and σ_{ap} as a function of wind speed and direction

Both σ_{sp} and σ_{ap} decreased with increasing wind speed (WS) when WS was > 2 m/s (Figure S7a and c). The three quartals (medians and 25th and 75th percentiles) decreased exponentially WS increased. An exponential function $y = C \cdot exp(-k \cdot WS)$ was fitted to the three quartals. The decay constant k for both $\sigma_{sp, median}$ and $\sigma_{ap, median}$ is 0.19 s m^{-1}, indicating both light scattering and absorption decreased by ~17.5% when WS increased by 1 m/s. Since σ_{sp} and σ_{ap} decreased at the same rate, SSA remained close to constant as a function of WS.

The three quartals of σ_{sp} and σ_{ap} also varied with wind direction (WD) (Figure S7b and S7d) and they have evidently different distributions, in agreement with Fig. 6 of the main article. The major differences in the directional dependency of σ_{sp} and σ_{ap} were around 165° and 285°. The median scattering coefficient for WD ~290° was around 500 Mm^{-1}, 50% higher than the median value of all directions (326 Mm^{-1}). Median σ_{ap} for WD ~160° is around 40 Mm^{-1}, almost as twice as high as the median value of all directions (21 Mm^{-1}).
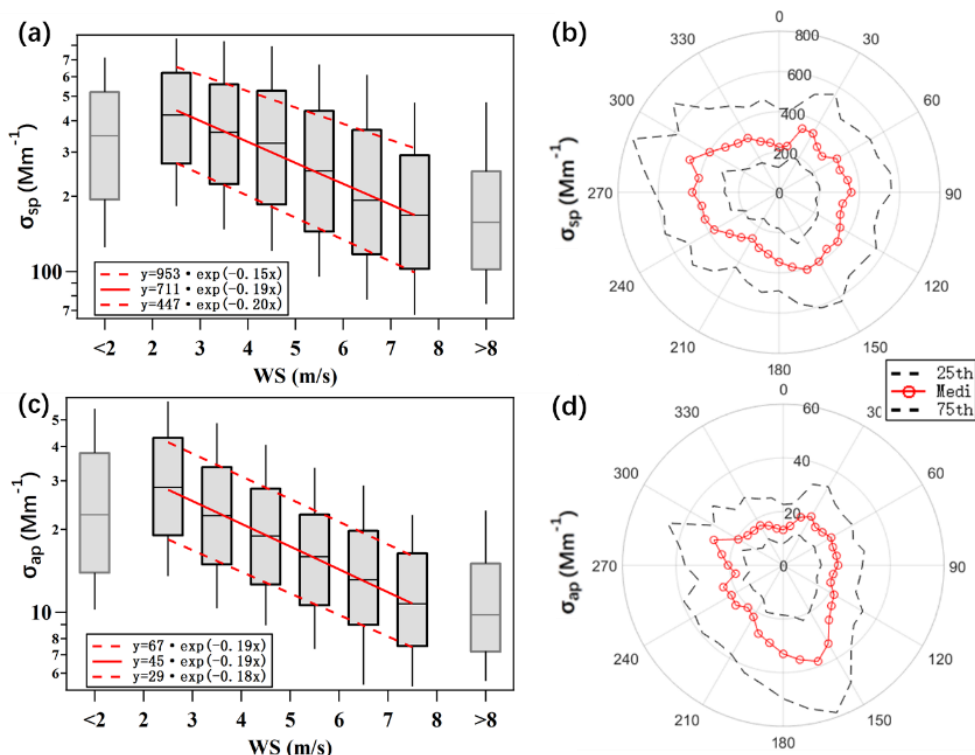

Figure S7. Relationship between σ_{sp} and σ_{ap} and wind speed and direction. (a) and (c): σ_{sp} and σ_{ap} as a function of wind speed. The solid lines represent medians, the boxes the 25th and 75th percentiles and the whiskers represent the 10th and 90th percentiles in each WS bin of 1 m/s. The red lines are fittings for 25th, 75th percentiles and medians. (b) and (d): σ_{sp} and σ_{ap} in 10° wind direction sectors. The red lines with circles represent medians and black dashed lines the 25th and 75th percentiles in each sector.

S7.2 Potential effect of biomass burning as an explanation for high σ_{sp} from WNW

Aged biomass burning aerosol tends to feature with higher scattering coefficient and single scattering albedo (e.g., Reid et al., 2005). To estimate whether the high σ_{sp} and SSA in the WNW sector could be explained by biomass burning events the concentrations of water-soluble ions (WSIs) in $PM_{2.5}$ were investigated. WSIs were measured at SORPES in the same period using a MARGA, see details of the measurements by Xie et al. (2015). Chemical composition is not the major focus of the present study so figures of wind dependence of aerosol chemical composition will not be presented anywhere in this paper except for Ca^{2+} and K^+ (Fig. S8c and S8d). K^+ concentration was slightly higher in WNW compared to adjacent wind directions (Fig. S8d), while the ratio between K^+ and σ_{sp} (or $K^+/PM_{2.5}$) was lower than average in this direction (not presented in a figure). K^+ is a primary component in aerosol. When compared K^+ with other primary components in $PM_{2.5}$, we found that K^+/Ca^{2+}, K^+/BC, K^+/Mg^{2+}, etc. were higher in WNW direction than average. The higher ratio between K^+ and other primary component and a lower ratio between K^+ and total $PM_{2.5}$ suggests that biomass burning may have contributed to the high scattering in this wind sector. However, the high scattering in this sector was observed in winter and the biomass burning season is in late spring and early summer so it is not likely that biomass burning explains the observations.
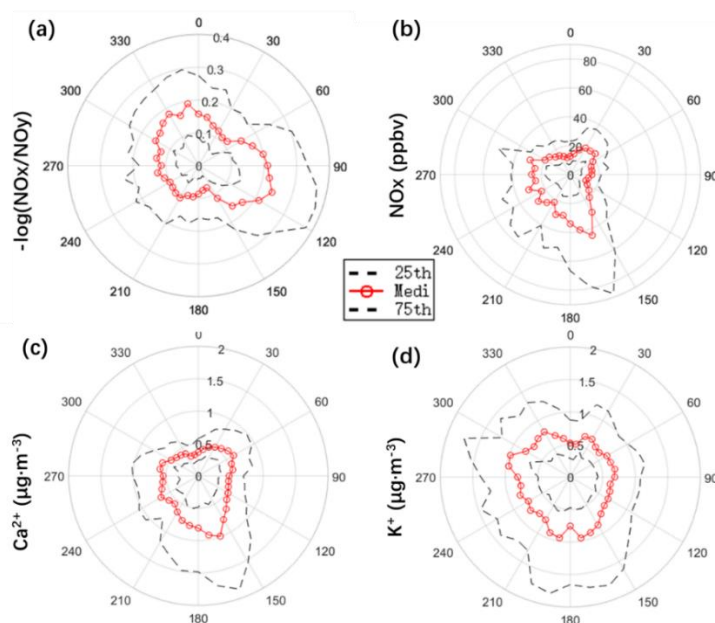

Figure S8. Medians, 25th and 75th percentiles of (a) photochemical age $= -\log(NO_x/NO_y)$, (b) NO_x concentrations (c) Ca^{2+} and (d) K^+ concentrations in $PM_{2.5}$ in 10° wind direction sectors.

S7.3 Explanations for high σ_{ap} from SSE

Figures S8a - c show the medians and quartals of photochemical age (i.e., $-\log(NO_x/NO_y)$), NO_x and Ca^{2+} concentrations as a function of wind direction. A significantly higher concentration of NO_x is a good indicator of vehicle emission especially when σ_{ap} is also evidently high. The photochemical age of air in the SSE sector is considerably lower than in other directions, suggesting that such emissions are close to SORPES. However, there is only one main road in the south of SORPES (~1.5 km away), and the traffic flow is not very large, not even closely comparable with the expressway to the west of SORPES. Traffic on this road cannot be the primary explanation of the high σ_{ap} and NO_x. We search an explanation with the diurnal variations of wind, NO_x and aerosols.

S7.3.1 Effect of diurnal variation of wind direction

The frequency of wind from SSE was significantly higher during nighttime and early morning. As discussed in the main article (chapter 3.2), both σ_{sp} and σ_{ap} were higher at nighttime and in the early morning. The variation of σ_{ap} was also stronger than σ_{sp} which may partly explain the evidently higher σ_{ap} and slightly higher σ_{sp} in the SSE wind sector.
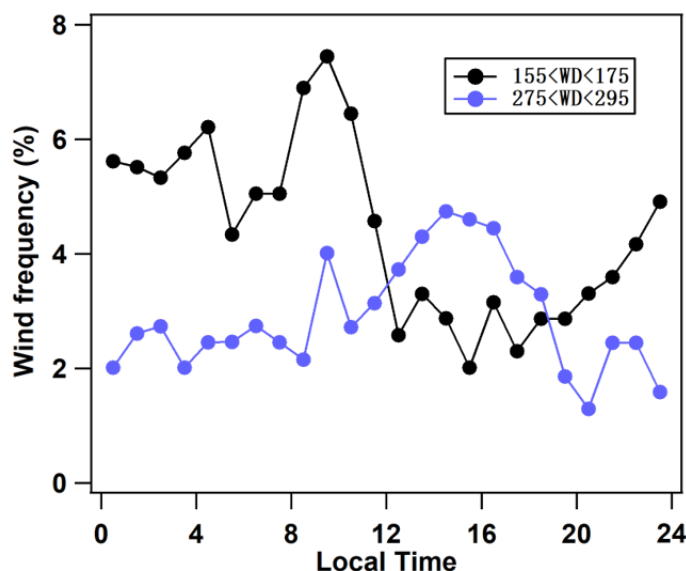

Figure S9. Diurnal variation of wind frequency at two given wind sector (WNW and SES)

S7.3.2 Evidence of vehicle emission from country roads

Ca^{2+} is usually a good indicator of soil dust. SORPES is located in the eastern part of China, the long-range-transport of dust is essentially impossible to come from the SSE direction. The high Ca^{2+} concentration from that sector is likely to be caused by local dust emissions. There is a large rural area to the south and south-east of SORPES. A further investigation shows that there are dozens of small factories and mines located within the area. Most of their locations are to the ESE of SORPES and their distance to SORPES are 3~10km. Those factories and mines need lots of heavy vehicles (mostly dumper truck) to transport their products. Roads inside the area are mainly poorly-maintained dirt roads, and when heavy vehicle drives on them, huge amounts of road dust rise. If there are enough vehicles driving on these roads, there will be high BC, high NO_x and high Ca^{2+} concentrations in air at the same time.

S7.3.3 Diurnal cycle of road emissions from the SSE sector

NO_x and Ca^{2+} concentrations were much higher at night (Figure S10). Further, the extent of diurnal variation was much more evident in the SSE sector (155°-175°) than in the overall data. This is consistent with the policy of the local government on vehicles. Dumper trucks are banned in entire Nanjing during the daytime, and they are only allowed at nighttime. The ratio $Ca^{2+}/PM_{2.5}$ at midnight is about two times higher than at noon. Since dust concentrations may also rise with strong wind, we also investigated wind speed. The result in figure S10b rules out this possibility as wind speed from SSE was usually lower during nighttime.
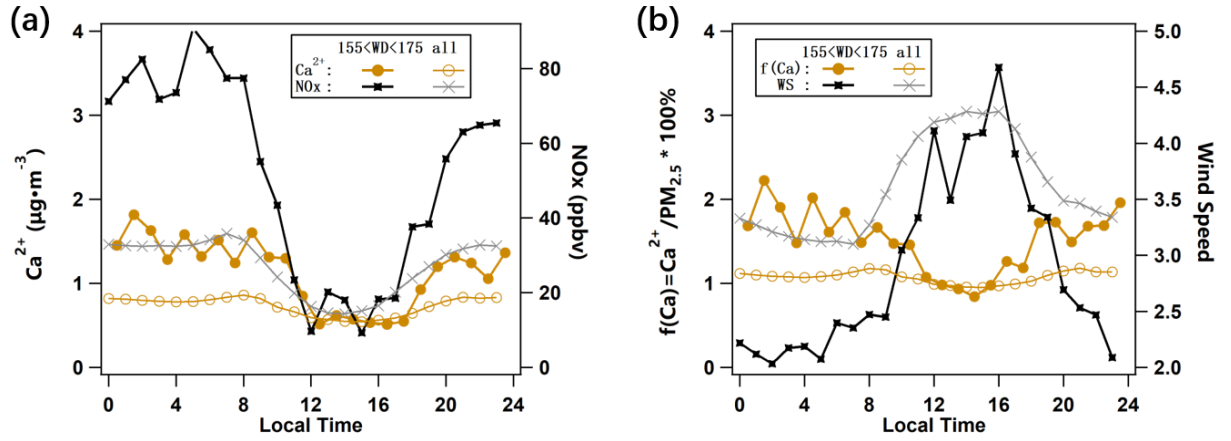
Figure S10. Diurnal cycle of (a) Ca^{2+} and NO_x concentrations; (b) fraction of Ca^{2+} in $PM_{2.5}$ = $f(Ca^{2+})$ and wind speed in SSE section and all wind section

To sum up, the analysis suggests the main cause for the high σ_{ap} during winds from the SSE sector is the nighttime heavy traffic on country dirt roads to several small factories and mines located within about 3 ~10 km to the ESE of SORPES.
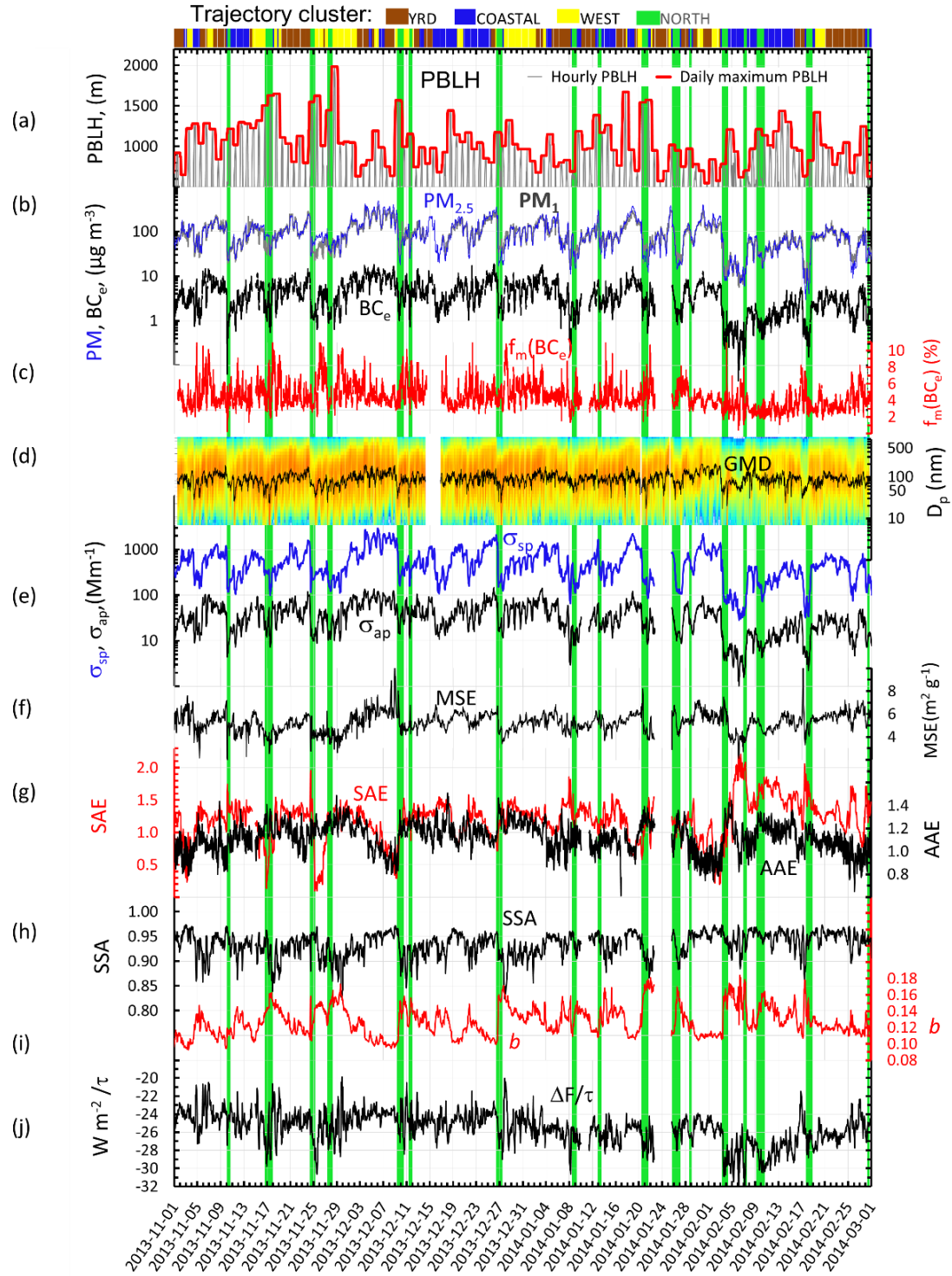
Figure S11. Same as Fig 9. but for the 4-month period 2013/11/01 – 2014/02/28. Hourly-averaged aerosol optical properties, mass concentrations and modeled boundary layer height during the polluted 4-month period